

AIMC-Spec: A Benchmark Dataset for Automatic Intrapulse Modulation Classification under Variable Noise Conditions

Sebastian L. Cocks, Salvador Dreo, and Feras Dayoub

Abstract—A lack of standardized datasets has long hindered progress in automatic intrapulse modulation classification (AIMC)—a critical task in radar signal analysis for electronic support systems, particularly under noisy or degraded conditions. AIMC seeks to identify the modulation type embedded within a single radar pulse from its complex in-phase and quadrature (I/Q) representation, enabling automated interpretation of intrapulse structure. This paper introduces AIMC-Spec, a comprehensive synthetic dataset for spectrogram-based image classification, encompassing 33 modulation types across 13 signal-to-noise ratio (SNR) levels. To benchmark AIMC-Spec, five representative deep learning algorithms—ranging from lightweight CNNs and denoising architectures to transformer-based networks—were re-implemented and evaluated under a unified input format. The results reveal significant performance variation, with frequency-modulated (FM) signals classified more reliably than phase or hybrid types, particularly at low SNRs. A focused FM-only test further highlights how modulation type and network architecture influence classifier robustness. AIMC-Spec establishes a reproducible baseline and provides a foundation for future research and standardization in the AIMC domain.

I. INTRODUCTION

Efficient and accurate analysis of electromagnetic signals is critical to a wide range of modern applications, including spectrum monitoring, cognitive electronic warfare, and other advanced signal processing systems. These tasks often involve detecting, classifying, and interpreting signals in complex and noisy environments. Typically, raw electromagnetic emissions are captured as I/Q data, which can then be processed into Pulse Descriptor Words, encoding features such as frequency, pulse width, and time of arrival, or transformed into time–frequency spectrograms for visual and algorithmic analysis. These representations form the basis of automated techniques for identifying signal characteristics and modulation types, enabling reliable performance in dynamic spectral conditions [1], [2], [3], [4], [5].

One critical classification task in this context is AIMC—the process of identifying the modulation scheme contained within a single radar pulse from its complex baseband representation. Formally, given a discrete I/Q sequence

$$x[n] = I[n] + jQ[n], \quad n = 1, 2, \dots, N$$

where each pulse p_i within $x[n]$ possesses an underlying modulation type m_i , the objective of AIMC is to estimate

S. L. Cocks and F. Dayoub are with Adelaide University, Adelaide, SA 5005 AUS (e-mail: sebastian.cocks@adelaide.edu.au).

This work is published in IEEE Access DOI: 10.1109/ACCESS.2025.3645091

the corresponding labels \hat{m}_i such that $\hat{m}_i \approx m_i$ for all pulses $p_i \in x[n]$. In practical terms, this involves transforming the I/Q data into a suitable time-frequency representation and applying a classification model to determine the modulation type present.

AIMC is a specialized sub-problem of radar modulation classification focused on intrapulse characteristics rather than interpulse or emitter-level behavior. Its correct formulation is essential for building robust radar signal analysis and electronic intelligence systems.

Prior to the emergence of deep learning, AIMC methodologies primarily followed a two-step process: feature extraction and classification. Feature extraction involved techniques such as time-frequency transformations (e.g., STFT, WVD, CWD) and statistical analyses to isolate and represent key signal characteristics [6], [7]. These features were then input into classifiers like SVMs, k-NN, or probabilistic models [8]. While these traditional methods provided foundational insights, they often required extensive domain knowledge and struggled with low SNR conditions, limiting their robustness and scalability.

While there has been progress in applying deep learning and image-based classification to AIMC, the field lacks a standardized, publicly available benchmark dataset. Most existing studies rely on private or internally generated data with limited transparency, making fair comparisons and reproducibility difficult.

This paper introduces a new synthetic dataset designed for benchmarking AIMC using spectrogram-based image classification methods. It includes a diverse collection of modulation types, including both radar and communication waveforms, and covers a wide range of SNR levels to support consistent and structured evaluation. The dataset is fully synthetic, allowing complete control over pulse parameters and noise levels while ensuring consistent ground-truth labels. This design isolates algorithmic performance from hardware-specific or environmental variables. To demonstrate the dataset’s practical utility, five representative deep learning algorithms from recent AIMC literature were selected, re-implemented, and benchmarked under varied signal conditions, enabling comparative analysis across architectures, modulation types, and noise levels. A focus of this work is on how different deep learning architectures respond to a common spectrogram representation of radar signals, rather than on comparing transform or preprocessing strategies. This framing ensures that observed performance differences reflect architectural design rather than input representation bias.

A. Contributions

- This work addresses a major gap in the AIMC field by introducing a publicly available synthetic dataset, AIMC-Spec, designed specifically for benchmarking image-based classification models. It includes 33 distinct intrapulse modulations and standardized signal definitions to support consistent comparison across future studies.
- Benchmarking results are provided using five diverse AIMC approaches, covering varied modeling strategies and preprocessing pipelines. These evaluations span 13 SNR levels, with an additional focused assessment on FM-only classification to isolate model performance under constrained conditions.
- All data and code are openly accessible for reproducibility and future research: <https://www.kaggle.com/sebastiancocks/datasets?query=aimc-spec> and <https://github.com/seb-cocks/AIMC-image-classification>

II. RELATED WORK

Research in AIMC has increasingly turned to deep learning, leveraging image-based representations of radar signals for robust classification under noisy and complex conditions. A broad range of models have been proposed, often distinguished by their architectural design, spectrogram generation techniques, and strategies for handling noise. While several datasets have been developed for radar or communication signal analysis, the AIMC field continues to lack a standardized, task-specific dataset to support fair and reproducible benchmarking.

Notable datasets such as RadarCommDataset [9], RadChar [10], and RadioML [11] include, but are not limited to, intrapulse modulations like linear frequency modulated (LFM), Barker and binary phase shift-keying (BPSK). However, they are not tailored to the AIMC problem. These resources often provide limited modulation coverage, do not consistently define signal structures, or focus more broadly on mixed communication and radar domains. As a result, despite their value, they fall short of supporting the reproducibility and comparability needed for rigorous AIMC evaluation. The development of a dedicated, well-documented AIMC dataset remains a necessary step to advance the field.

Several studies have focused on refining input quality through spectrogram preprocessing. Wang et al. [1], proposed a lightweight CNN model using Short-Time Fourier Transform (STFT) spectrograms enhanced by multi-stage zero-mean scaling and noise reduction, achieving 96.7% accuracy at an SNR of -6 dB across 6 modulation types. He et al. [12], used Continuous Wavelet Transform (CWT) to produce high-resolution time-frequency images, reaching 90% accuracy at -11 dB with a compact CNN evaluated on 12 modulation types. The work of Kong et al. [13] introduced the Fourier synchrosqueezing transform (FSST) in place of Choi-Williams Distribution (CWD), applying complex-valued spectrograms for CNN classification and attaining

98.4% accuracy at -10 dB on 8 modulation classes. The LPI-Net model, developed by Huynh-The et al. [14], utilized CWD spectrograms in a modular CNN built from asymmetric convolutional paths and skip connections, achieving 98.6% accuracy at 0 dB across 13 modulation types. Across these studies, all models were trained on custom datasets that were not made publicly available. Reported accuracies ranged from 90% to 98.6%, typically evaluated at SNR levels between -11 dB and 0 dB , with class counts ranging from 6 to 13.

Other studies incorporated denoising mechanisms into the learning pipeline. The approach by Qu et al. [2] combined a Convolutional Denoising Autoencoder (CDAE) with an Inception-based CNN to denoise Cohen's Class Distribution (CTFD) inputs, achieving over 95% accuracy at -9 dB across 12 modulation types. A DenseNet classifier in conjunction with a CDAE was proposed by Yang et al. [15], reaching 99.6% accuracy at -6 dB and 92% at -10 dB on 6 modulation classes using STFT spectrograms. The LDC-Unet model by Jiang et al. [4] integrated a U-Net feature extractor with local dense connections and a fine-tuned VGG-19 classifier trained with a custom SSR-loss function, achieving 91.17% accuracy at -10 dB across 12 modulation types. All three studies used custom datasets that were not made publicly available. Reported accuracies ranged from 91.17% to 99.6%, with evaluations commonly conducted at SNR levels between -10 dB and -6 dB , covering 6 to 12 modulation classes.

Transformer components and attention mechanisms have also emerged in recent architectures. RM-Net of Tang et al. [5] combined ResNet blocks with multi-head self-attention and SCR-loss on CWD spectrograms, achieving 95.5% accuracy at -10 dB across 12 modulation types. The method by Shen et al. [16] employed a parallel residual CNN trained on CWD spectrograms under multi-path fading environments, reporting 81% accuracy at -10 dB on 12 classes. Both studies evaluated performance on private datasets that were not publicly released. Despite the architectural differences, they shared common evaluation conditions—namely, 12 modulation types and low-SNR scenarios centered around -10 dB —highlighting their focus on robustness under challenging channel conditions.

Additional strategies include multi-label classification and joint learning. Qu et al. [3] used Deep Q-Learning with custom CTFD kernels, achieving 94.5% accuracy at -6 dB across 8 modulation types. A DnCNN-ResNet pipeline for aliasing-resilient multi-label classification was presented by Hong-hai et al. [17], reporting 97% accuracy at 0 dB on 5 classes. The approach of Li et al. [18] employed Kernel Collaborative Representation and Discriminative Projection alongside a fine-tuned CNN, reaching 97.58% at -6 dB across 12 modulation types. A semi-hard triplet loss and SER block-based method was introduced through Qu et al. [19], achieving 88% accuracy at -10 dB for unknown radar signal recognition across 14 modulation types. These models were all evaluated using internal datasets that were not publicly shared. Accuracy levels ranged from 88% to 97.58%, with class counts varying widely—from 5 to 14—depending on

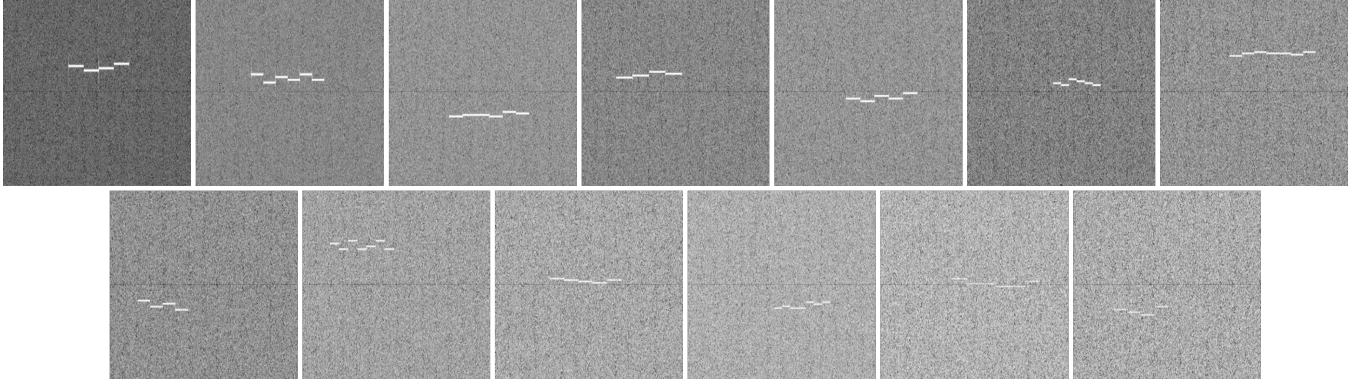


Fig. 1. Spectrograms of a 4-frequency shift-keying (4FSK) signal across all SNR levels in AIMC-Spec, ranging from +10 dB (top left) to -20 dB (bottom right). SNR initially decreases in 5 dB steps from +10 to 0 dB and then alters to 2 dB steps from 0 to -20 dB. The progression illustrates the degradation of time-frequency structure as noise increases.

whether the task targeted known, unknown, or overlapping signal types.

Recent work by Bhatti et al. [20] explored transformer-based architectures for recognizing phase-coded radar waveforms under extremely low SNR conditions. Their study proposed three AMRS models—ViT, Vicinity ViT (VViT), and a CNN baseline—trained on phase spectrograms derived from STFT. Focusing on six types of phase-coded signals—Barker, Frank, and Polyphase 1–4 (P1–P4)—they demonstrated robust recognition at SNRs as low as -16 dB. The VViT model achieved a recognition accuracy of 93% at -16 dB, outperforming ViT (92.7%) and CNN (89%). By leveraging phase information rather than magnitude, this work highlights the potential of transformer-based models in ultra-low SNR AIMC scenarios.

From this broad survey, five representative approaches [1], [14], [2], [4], [20] were selected for benchmarking. These encompass lightweight CNNs, denoising autoencoders, modular convolutional pipelines, fine-tuned pretrained backbones, and transformer-based networks, capturing the methodological diversity of AIMC research and enabling comparative evaluation on a consistent dataset.

Despite these promising developments, the lack of common datasets and inconsistencies in reported signal definitions, SNR conditions, and generation methods continue to impede progress. Tables I, II and III illustrates the limited overlap in modulation types across studies, emphasizing the need for standardized datasets to ensure fair comparison and reliable benchmarking.

A. Case for New Dataset

Despite the range of deep learning approaches applied to AIMC, nearly all rely on custom datasets that are not publicly available. These datasets vary in modulation class count, SNR range, and preprocessing methods, making fair comparison and reproducibility difficult. Reported results span from 5 to 14 classes and SNRs from 0 dB to -11 dB, with no consistent evaluation standard across studies.

While existing resources like RadarCommDataset [9], RadChar [10], and RadioML [11] offer intrapulse modula-

tions, they are not designed for AIMC. Their broader focus and inconsistent definitions limit their use for benchmarking intrapulse classification tasks. To address these gaps, this paper introduces AIMC-Spec: a dedicated dataset for reproducible, standardized evaluation of AIMC methods.

III. DATA SET PROPERTIES

AIMC-Spec is divided into 13 SNR levels, each containing 33 intrapulse modulations with 1,000 signals per modulation. Signals were generated via a Python script that automatically selected parameters relevant to each modulation type. This section outlines the key dataset attributes, including signal configurations, noise conditions, modulation types, and file organization.

A. Pulse and Modulation Parameter Selection

Each signal consists of 100,000 samples, corresponding to a simulation time of 1 ms, sampled at 100 MHz. The Python-based generator assigned parameters such as carrier frequency, pulse width, and time of arrival randomly within predefined bounds. The carrier frequency was selected randomly within a 50 MHz range and applied to modulate the baseband signal.

B. Signal to Noise Ratio (SNR)

As the dataset is synthetically generated, it lacks natural noise. To approximate real-world conditions, Additive White Gaussian Noise (AWGN) was applied after signal generation. AWGN was chosen because it effectively models thermal noise, which is commonly encountered in communication systems due to its random and uniformly distributed characteristics across all frequencies. The dataset includes 13 SNR levels: +10, +5, and a range from 0 to -20 dB in steps of 2. Specifically: +10, +5, 0, -2, -4, -6, -8, -10, -12, -14, -16, -18, -20 dB.

Noise was added directly to the raw pulse before spectrogram transformation, using a fixed noise power reference of 1 dB. An SNR of 0 dB signifies parity between signal and noise power. Figure 1 presents spectrograms of a representative signal between +10 and -20 dB, illustrating the effect of

TABLE I

FM CLASS USAGE ACROSS REFERENCED STUDIES. EACH ROW REPRESENTS A MODULATION TYPE AND EACH COLUMN A CITED PAPER. FILLED CELLS INDICATE THE MODULATION WAS INCLUDED IN THAT STUDY; EMPTY CELLS INDICATE IT WAS NOT.

	AIMC-Spec	[12]	[14]	[17]	[4]	[13]	[18]	[3]	[2]	[19]	[16]	[5]	[1]	[15]	[21]	[22]	[23]	[24]	[25]	[26]	[27]	[28]	[20]
UNMOD																							
LFM																							
NLFM																							
SFM																							
EQFM																							
DLFM																							
MLFM																							
2FSK																							
4FSK																							
SINFM																							
TRIFM																							
SCR																							
PCR3																							
QFSK																							

TABLE II

PHASE MODULATION CLASS USAGE ACROSS REFERENCED STUDIES. EACH ROW REPRESENTS A MODULATION TYPE AND EACH COLUMN A CITED PAPER. FILLED CELLS INDICATE THE MODULATION WAS INCLUDED IN THAT STUDY; EMPTY CELLS INDICATE IT WAS NOT.

	AIMC-Spec	[12]	[14]	[17]	[4]	[13]	[18]	[3]	[2]	[19]	[16]	[5]	[1]	[15]	[21]	[22]	[23]	[24]	[25]	[26]	[27]	[28]	[20]
BPSK																							
QPSK																							
FRANK																							
BARKER																							
COSTAS																							
P1-4																							
T1-4																							

TABLE III

MODULATION CLASS USAGE ACROSS REFERENCED STUDIES. EACH ROW REPRESENTS A MODULATION TYPE AND EACH COLUMN A CITED PAPER. FILLED CELLS INDICATE THE MODULATION WAS INCLUDED IN THAT STUDY; EMPTY CELLS INDICATE IT WAS NOT.

	AIMC-Spec	[12]	[14]	[17]	[4]	[13]	[18]	[3]	[2]	[19]	[16]	[5]	[1]	[15]	[21]	[22]	[23]	[24]	[25]	[26]	[27]	[28]	[20]
LFM-BPSK																							
2FSK-BPSK																							
LFM-SFM																							
BPSK-LFM																							
EQFM-BPSK																							
EQFM-2FSK																							
FRANK-EQFM																							
FRANK-4FSK																							
LFM-4FSK																							
BPSK-FSK																							
FSK-LFM																							
FSK-BPSK																							

noise on visual clarity. While AIMC-Spec currently models only AWGN, future releases will incorporate additional channel effects—such as multipath propagation, fading, and pulse jitter—to emulate real-world radar conditions more closely.

C. Intrapulse Modulations

AIMC-Spec includes 33 intrapulse modulation types grouped into frequency (13), phase (17), and hybrid (3) categories. These modulation types also serve as the class labels for classification tasks. FM signals are often visually distinct in spectrograms due to frequency sweeps. In contrast, phase modulations (PM) and hybrid modulations (HM) produce more subtle patterns—phase shifts introduce discontinuities or faint texture shifts that are less salient to image-based classifiers.

D. Data Set Structure

The dataset is stored in 13 folders, each storing 33 binary .h5 files—one per intrapulse modulation—using Python’s h5py module. Each file contains 1,000 pulses per class with a single pulse including 100,000 I/Q samples along with

associated metadata. Each .h5 file is approximately 1.18 GB in size, with each SNR folder being 37 GB, making the whole data set 482 GB.

IV. BENCHMARK ALGORITHMS

A curated selection of five algorithms was chosen to benchmark AIMC-Spec, reflecting both their influence in the field and their architectural diversity. The set spans convolutional, denoising, U-Net-like, pretrained, and transformer architectures, ensuring that different feature-extraction paradigms are represented. Each has demonstrated strong performance in prior studies under varying SNR conditions. Collectively, these models form a balanced cross-section of contemporary AIMC research and provide insight into how distinct neural architectures handle a common spectrogram representation. Figure 2 shows the preprocessing outputs for each model on a 4FSK signal at 0 dB SNR, with architectural summaries provided in Appendix VII (Figures 7–10).

A. LDC-Unet: Unet + VGG19

The method in [4] employs the Smooth Pseudo-Wigner Ville Distribution (SPWVD) to generate time-frequency images, which are resized to 128×128 using bicubic interpolation—an approach that averages pixel values across a neighborhood for smooth visual scaling. The model combines a modified U-Net with local dense connections and a fine-tuned VGG-based deep CNN. It is trained using a custom SSR Loss and optimized via stochastic gradient descent (SGD). An example of the resulting spectrogram is shown in Figure 2(b).

B. LPI-Net: Modular Lightweight CNN

The architecture in [14] uses the CWD for spectrogram generation. As with LDC-Unet, outputs are resized to 64×64 using bicubic interpolation and converted to grayscale. The model is a modular CNN composed of repeated convolutional blocks, trained using cross-entropy loss and optimized with SGD. Its grayscale pipeline and modular design contribute to its computational efficiency. The preprocessed 4FSK example is displayed in Figure 2(c).

C. CDAE-DCNN: Denoising Auto-Encoder + DCNN

In [2], spectrograms are produced using the CTFD, resized to 64×64 via linear interpolation, and normalized. A convolutional denoising autoencoder first removes noise from the spectrograms, which are then passed to a deeper CNN for classification. The model uses the Adam optimizer with standard cross-entropy loss. The denoised spectrogram output is shown in Figure 2(d).

D. STFT-CNN: Simple CNN

The approach in [1] uses the simplest architecture in the benchmark set, comprising only 5 layers—the fewest among all models compared. It generates spectrograms via the STFT, resizes them using pixel area interpolation, and applies normalization. An iterative noise suppression step is used before classification by a lightweight CNN trained with Adam and cross-entropy loss. The corresponding spectrogram image is presented in Figure 2(e).

E. ViT: Phase-Spectrum Vision Transformer

The ViT model from [20] operates on phase spectrograms extracted via the STFT, focusing on the carrier-aligned phase row (typically the seventh) to form compact one-dimensional images that capture phase variations over time. Because only this single frequency row corresponding to the carrier is retained, the resulting phase-spectrum image is inherently non-square rather than the conventional $N \times N$ time-frequency map. This compact 1D representation significantly reduces computational complexity while preserving modulation-specific phase patterns. These cropped phase spectra are divided into 23-sample patches and passed through eight transformer layers with four attention heads. A learnable classification token and multilayer perceptron head perform the final prediction. Trained using cross-entropy loss and the AdamW optimizer, the model achieves over

92% accuracy at -16 dB on six phase-coded modulations. A sample non-square input is shown in Figure 2(f).

Together, these algorithms represent a diverse set of modeling strategies, ranging from lightweight CNNs to transformers, covering the breadth of contemporary AIMC techniques.

V. EXPERIMENTING AND BENCHMARKING

A. Methodology

This study benchmarks five representative AIMC algorithms using a unified FFT-based spectrogram pipeline implemented with open-source signal-processing tools. Each model was trained and tested using the same spectrogram input type to ensure consistency and isolate architectural performance. Several prior works lacked sufficient methodological detail or were designed for markedly different data conditions (e.g. short I/Q segments rather than full-scale pulse windows). In addition, attempts to directly apply those transforms to the AIMC-Spec signals produced distorted or invalid time-frequency images. Using an FFT-based approach with 50% window overlap provides stable, reproducible inputs and practical runtime.

While other time-frequency transforms such as CWD, SPWVD, and FSST can yield richer-time frequency resolution, these were intentionally excluded to prevent confounding architectural comparison with transform-specific effects. Standardizing on the FFT transform isolates model behavior from representation specific tuning, aligning with a primary objective of this work—to examine how distinct neural architectures (CNN, UNet, ViT, etc.) perform on the AIMC-Spec dataset under identical input conditions. A follow-up study will explore how alternative transforms influence model performance on AIMC-Spec.

B. Implementation

All spectrograms were generated using the open-source cupy Python library to accelerate FFT computation on GPU. A consistent 80:20 train-test split was applied to each model. Original loss functions and optimizers were preserved as described in their respective source papers.

Training was performed on an NVIDIA GeForce RTX 4090 GPU using a batch size of 32. Each model trained for up to 200 epochs, with early stopping (patience of 50 epochs) to prevent overfitting. During training, loss histories were recorded for each run. Final model evaluations included overall classification accuracy and confusion matrix generation.

C. Experiments

Two core experimental setups were designed to evaluate model performance under controlled and variable noise conditions. The first setup trained and tested each model on the same SNR level (denoted as $\text{SNR}(x):\text{SNR}(x)$), assessing performance when the noise environment remains consistent. The second setup trained on a combined dataset spanning all

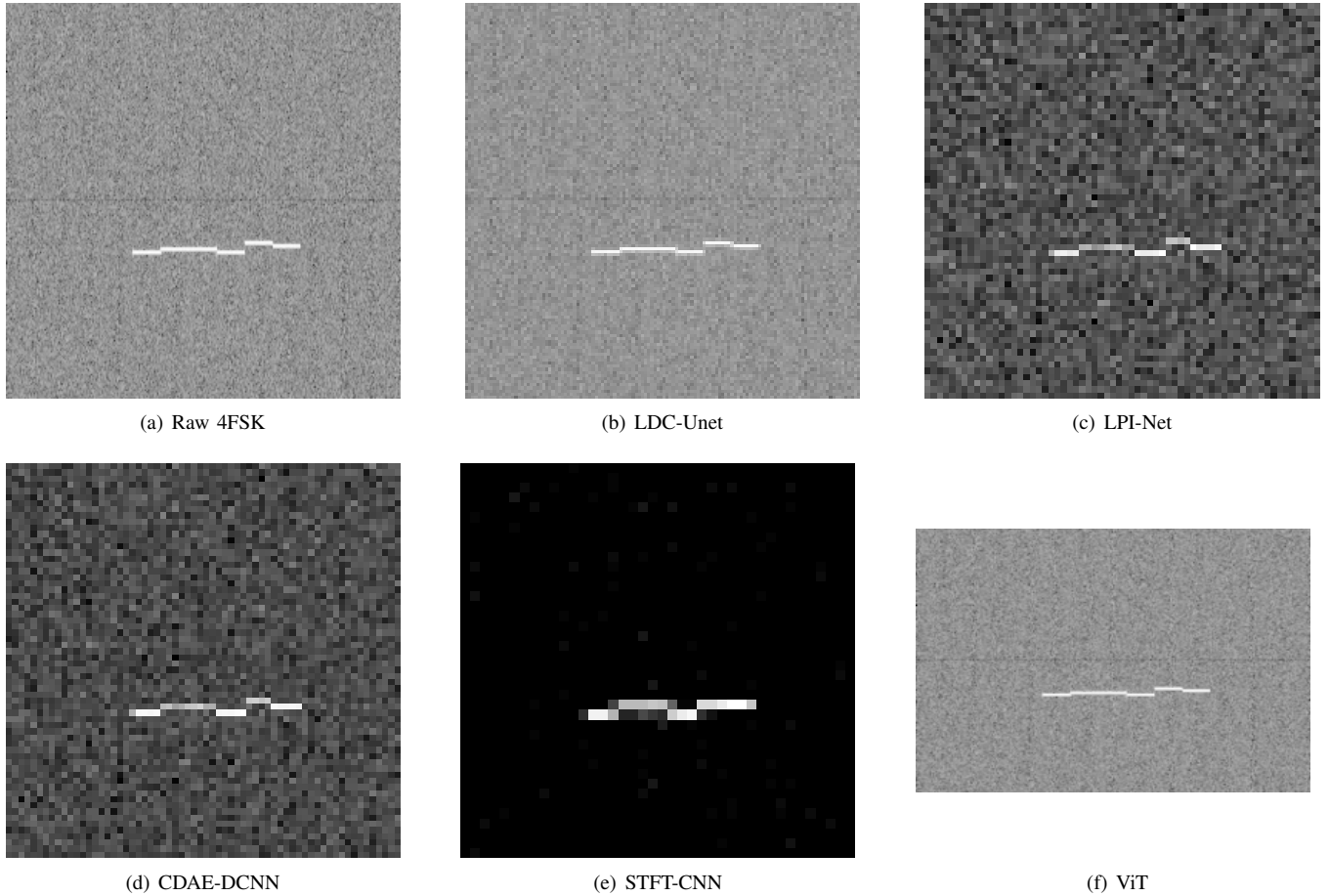


Fig. 2. Spectrogram representations of the 4FSK modulation at 0 dB SNR following preprocessing by the six benchmark algorithms. Each spectrogram was generated using a 256-point Hann window with 50 % overlap.

SNR levels (+10 dB to -20 dB) and tested on individual levels (SNR(ALL):SNR(x)), measuring each model's capacity to generalize under unseen noise intensities.

Each experimental setup was repeated in two variants. The first included all 33 intrapulse modulation types to assess full-spectrum performance. The second restricted the task to a subset of 13 frequency modulations, chosen for their well-defined spectral features and higher separability. This subset reflects the more tractable conditions often used in prior AIMC studies, where models are frequently benchmarked on modulation classes that produce visually distinct patterns in spectrograms. These two variants enable both a rigorous full-task benchmark and a focused evaluation under favorable modulation conditions.

D. Results

Algorithm Performance Across SNR Levels: LDC-Unet achieved the strongest performance across all evaluated conditions, including at -20 dB in both the SNR(ALL):SNR(x) and SNR(x):SNR(x) configurations. On the full modulation set, it reached 41.84% and 41.06% accuracy, respectively, while on the frequency-only (FM) subset, it attained 90.81% and 90.46%. These results are illustrated in Figures 3, 4, 5 and 6. Performance was consistently higher in the FM-only tests, reflecting the reduced complexity of this subset

compared to the full modulation classification task. Notably, LDC-Unet was the only model to maintain the top position across all experimental conditions, regardless of SNR configuration or modulation subset.

In the SNR(ALL):SNR(x) full-modulation experiment, LDC-Unet's average margin over the second-best model (ViT) was 11.27%, with a specific difference of 12.36 percentage points at -20 dB. On the FM subset of the same setup, the gap widened to 15.77 points. For the SNR(x):SNR(x) configuration, LDC-Unet led CDAE-DCNN by 16.03 percentage points on the full task and by 26.62 on FM. These differences indicate that LDC-Unet maintained a consistent and measurable advantage regardless of training condition or task type.

ViT ranked second in the SNR(ALL):SNR(x) setup, reaching 43.18% at 0 dB on the full set and 91.96% on FM, as shown in Figures 4 and 6. However, its performance dropped in the SNR(x):SNR(x) setup, with 26.85% on the full task and 51.58% on FM at 0 dB, suggesting a greater reliance on larger training datasets.

CDAE-DCNN achieved the second-best results in the SNR(x):SNR(x) experiments, with 40.38% on the full task and 90.35% on FM at 0 dB, outperforming both ViT and LPI-Net in this limited-data context, as shown in Figures 3

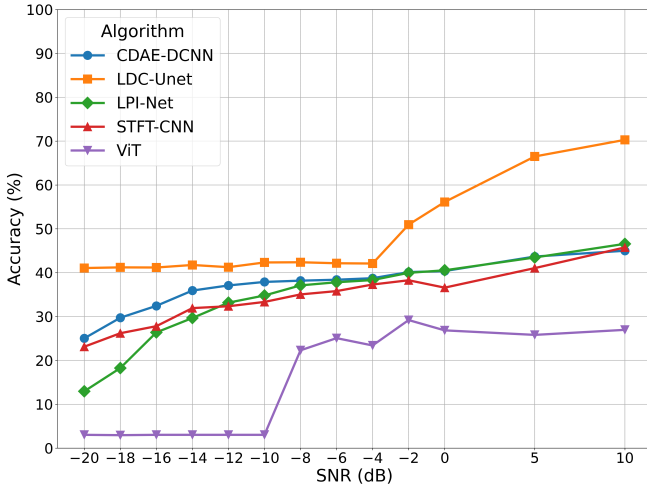


Fig. 3. Accuracy (%) vs SNR (dB) for experiment $\text{SNR}(x):\text{SNR}(x)$, using all modulation types.

and 5.

Across all models, FM classification yielded higher accuracy compared to the full modulation task. For example, in the $\text{SNR}(x):\text{SNR}(x)$ setup at -20 dB, LDC-Unet’s accuracy increased from 41.06% on the full modulation set to 90.46% on FM—a gain of over 49 percentage points. This large gap reinforces the relative ease of distinguishing frequency-only modulations and highlights the added challenge introduced by phase and hybrid types, particularly under high-noise conditions.

Algorithm Trends: LDC-Unet consistently reported the highest accuracy across SNR levels in nearly all experimental setups. CDAE-DCNN reported the second-highest accuracy in both the full and FM tasks under the $\text{SNR}(x):\text{SNR}(x)$ setting, while ViT achieved second-best results in the more data-rich $\text{SNR}(\text{ALL}):\text{SNR}(x)$ configuration. STFT-CNN showed relatively strong accuracy considering its compact architecture, demonstrating that competitive accuracy does not strictly require large parameter counts—particularly when paired with well-structured time-frequency inputs.

A notable trend was the disparity between model performance on frequency modulations (FM) versus the full 33-class task. While some models, such as CDAE-DCNN and LPI-Net, saw relatively modest gains, others—particularly ViT—showed substantial improvement. This suggests that ViT’s architecture benefits more from clean, distinct modulation classes and especially from larger datasets. Given that the $\text{SNR}(\text{ALL})$ training setup yields a 13-fold increase in data volume (due to 13 SNR levels), ViT’s improvement in that setting aligns with known transformer characteristics: large data quantities are essential for optimal performance.

Analytical Discussion: While overall accuracies provide a useful benchmark, deeper inspection of the accuracy–SNR trends in Tables IV–VII reveals distinct behavioral patterns that align with each algorithm’s design.

LDC-Unet maintained the highest stability across all noise conditions, with less than a 30% accuracy drop between

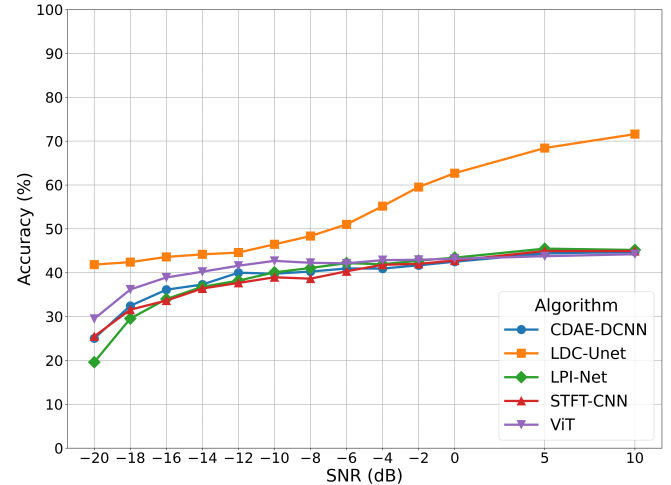


Fig. 4. Accuracy (%) vs SNR (dB) for experiment $\text{SNR}(\text{ALL}):\text{SNR}(x)$, using all modulation types.

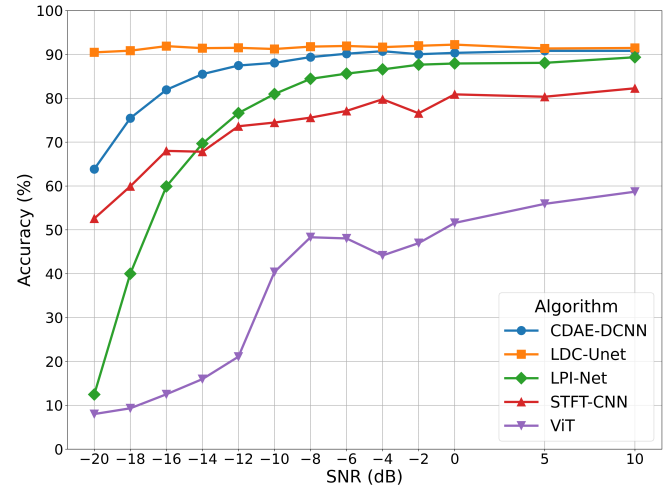


Fig. 5. Accuracy (%) vs SNR (dB) for experiment $\text{SNR}(x):\text{SNR}(x)$, using only frequency modulations.

+10 dB and -20 dB. This resilience stems from its local dense skip connections and residual encoder blocks, which preserve multi-scale features and reconstruct fine-grained spectrogram detail even when noise dominates the input. The use of SSR-loss further enforces intra-class compactness and inter-class separation, allowing the model to maintain discriminative boundaries under low-SNR degradation.

CDAE-DCNN also performed strongly at low SNRs due to its denoising pre-training stage. However, compared with LDC-Unet, it exhibited a steeper decline below -10 dB, consistent with the CDAE’s tendency to over-smooth high-frequency or phase-rich modulations. This explains its slight disadvantage in the full-modulation task despite high FM-only accuracy.

ViT achieved high accuracy in the data-rich $\text{SNR}(\text{ALL}):\text{SNR}(x)$ configuration but degraded rapidly in $\text{SNR}(x):\text{SNR}(x)$, reflecting its dependency on large and diverse training sets. The transformer’s global-attention

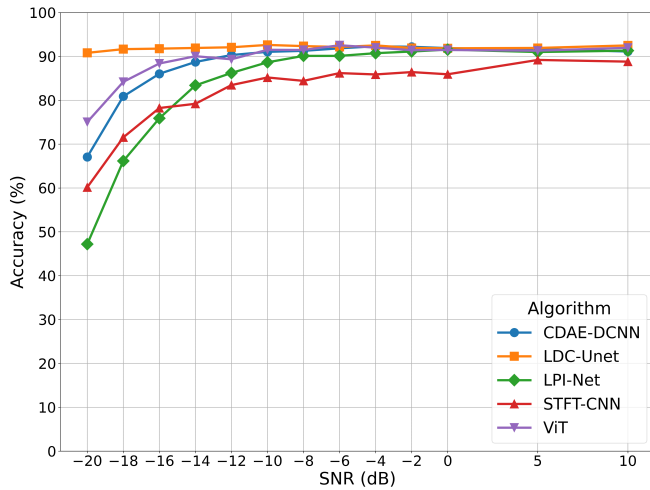


Fig. 6. Accuracy (%) vs SNR (dB) for experiment $\text{SNR}(\text{ALL}):\text{SNR}(x)$, using only frequency modulations.

mechanism generalizes well when abundant samples capture the full SNR spectrum, but without that diversity its performance becomes unstable—a known limitation of transformer architectures in small-sample radar tasks.

STFT-CNN and LPI-Net demonstrated consistent but modest performance, limited mainly by their input representations. STFT-CNN’s small receptive field and compact RGB images constrain the capture of long-term spectral patterns, while LPI-Net’s grayscale preprocessing reduces feature richness for overlapping or phase-coded signals. Nevertheless, both models highlight that well-structured spectrogram inputs can achieve competitive results even with lightweight CNNs.

Across all algorithms, frequency-only (FM) tasks consistently exceeded full-modulation performance by 40–50 percentage points at low SNRs. This disparity indicates that the principal challenge lies in recognizing phase and hybrid modulations, where spectral cues are less visually separable and inter-class boundaries overlap under noise. The different slopes of each model’s accuracy–SNR curve underscore architectural sensitivity to these factors: denoising or skip-connected models degrade smoothly, while attention-based and shallow CNNs show abrupt losses once noise dominates feature variance.

Collectively, these observations suggest that model behavior on AIMC-Spec is driven less by absolute accuracy and more by how effectively each architecture mitigates information loss under noise and class imbalance—insight critical for guiding future multi-frame and multi-modal designs.

Influence of Preprocessing and Input Design: The preprocessing choices and input formats—previously detailed for each algorithm—appeared to influence classification outcomes. Algorithms that preserved more visual detail through color or interpolation tended to achieve higher accuracy on more complex modulation types. For example, LDC-Unet and CDAE-DCNN were better able to retain phase and hybrid modulation characteristics, likely due to their use of

RGB inputs and larger spectrogram resolution.

By contrast, LPI-Net’s grayscale preprocessing likely reduced feature richness, particularly for modulations with overlapping frequency or phase behaviors. STFT-CNN, though using RGB inputs, was constrained by its very small image size, limiting its spatial feature representation. ViT, which received phase spectrogram inputs in a single-channel format, achieved lower accuracy in the $\text{SNR}(x):\text{SNR}(x)$ setting—again suggesting that the quantity and richness of training data have a disproportionate impact on transformer-based models compared to CNNs. These observations suggest that aligning input design with architectural characteristics may benefit performance in noisy environments.

VI. CONCLUSION

This paper presents AIMC-Spec, a synthetic dataset purpose-built for AIMC using spectrogram-based image classification techniques. It includes a diverse range of 33 intrapulse modulation types—spanning frequency, phase, and hybrid categories—across a wide SNR spectrum, allowing for rigorous and structured benchmarking under varied signal conditions.

Five representative deep learning algorithms were implemented and evaluated on AIMC-Spec, highlighting differing behaviors across model architectures. The results are consistent with known trends in AIMC: frequency modulations are generally more separable, while phase and hybrid types present greater challenges. The benchmarking demonstrates AIMC-Spec’s potential as a diagnostic tool for analyzing algorithm performance across modulation types and noise levels.

A. Future Works

Future work should extend AIMC-Spec to include additional modulation classes and finer grained SNR intervals to better assess model robustness in harsh conditions. Furthermore, more benchmarking algorithms, including those not originally designed for AIMC, should be explored to evaluate cross-domain generalizability.

Beyond architectural benchmarking, future iterations of AIMC-Spec will incorporate greater environmental realism by integrating measured or parameter-derived radar signals and by simulation operation effects such as multipath propagation, fading, pulse dropouts, phase jitter, and measurement noise. These additions will enable the dataset to emulate real-world conditions more accurately and provide a stronger basis for evaluating resilience and generalization performance.

With ongoing updates, AIMC-Spec can evolve into a lasting benchmark for the AIMC community. Its structured, transparent design enables reproducible research, fair comparisons, and clearer insights into model behavior—providing a foundation for future research in intrapulse modulation classification.

REFERENCES

[1] Xuebao Wang, Gaoming Huang, Zhiwen Zhou, and Jun Gao, “Radar emitter recognition based on the short time fourier transform and convolutional neural networks,” in *2017 10th International Congress on Image and Signal Processing, BioMedical Engineering and Informatics (CISP-BMEI)*. pp. 1–5, IEEE.

[2] Zhiyu Qu, Wenyang Wang, Changbo Hou, and Chenfan Hou, “Radar signal intra-pulse modulation recognition based on convolutional denoising autoencoder and deep convolutional neural network,” *IEEE Access*, vol. 7, pp. 112339–112347, 2019.

[3] Zhiyu Qu, Chenfan Hou, Changbo Hou, and Wenyang Wang, “Radar signal intra-pulse modulation recognition based on convolutional neural network and deep q-learning network,” *IEEE Access*, vol. 8, pp. 49125–49136, 2020.

[4] W. Jiang, Y. Li, M. Liao, and S. Wang, “An improved lpi radar waveform recognition framework with ldc-unet and ssr-loss,” *IEEE Signal Processing Letters*, vol. 29, pp. 149–153, 2022.

[5] Zeyu Tang and Hong Shen, “Improved radar signal recognition by combining resnet with transformer learning,” *2024 International Conference on Green Energy, Computing and Sustainable Technology (GECOST)*, pp. 94–100, 2024.

[6] Jingjing Cai, Fengming Gan, Xianghai Cao, Wei Liu, and Peng Li, “Radar intra-pulse signal modulation classification with contrastive learning,” *Remote. Sens.*, vol. 14, pp. 5728, 2022.

[7] Fatih Cagatay Akyon, Yasar Kemal Alp, Gokhan Gok, and Orhan Arikhan, “Classification of intra-pulse modulation of radar signals by feature fusion based convolutional neural networks,” *2018 26th European Signal Processing Conference (EUSIPCO)*, pp. 2290–2294, 2018.

[8] Shi Yuan, Bin Wu, and Peng Li, “Intra-pulse modulation classification of radar emitter signals based on a 1-d selective kernel convolutional neural network,” *Remote. Sens.*, vol. 13, pp. 2799, 2021.

[9] Anu Jagannath and Jithin Jagannath, “Dataset for modulation classification and signal type classification for multi-task and single task learning,” *Comput. Networks*, vol. 199, pp. 108441, 2021.

[10] Zi Huang, Akila Pemasiri, Simon Denman, Clinton Fookes, and Terrence Martin, “Multi-task learning for radar signal characterisation,” *2023 IEEE International Conference on Acoustics, Speech, and Signal Processing Workshops (ICASSPW)*, pp. 1–5, 2023.

[11] Timothy J. O’Shea, T. Roy, and N. West, “Over-the-air deep learning based radio signal classification,” *IEEE Journal of Selected Topics in Signal Processing*, vol. 12, no. 1, pp. 168–179, 2017.

[12] Peng He, Yang Zhang, Xinyue Yang, Xiao Xiao, Haolin Wang, and Rongsheng Zhang, “Deep learning-based modulation recognition for low signal-to-noise ratio environments,” *Electronics*, vol. 11, no. 23, pp. 4026, 2022.

[13] Guyyeol Kong and Visa Koivunen, “Radar waveform recognition using fourier-based synchrosqueezing transform and cnn,” *2019 IEEE 8th International Workshop on Computational Advances in Multi-Sensor Adaptive Processing (CAMSAP)*, pp. 664–668, 2019.

[14] Thien Huynh-The, Van-Sang Doan, Cam-Hao Hua, Viet Quoc Pham, Toan-Van Nguyen, and Dong-Seong Kim, “Accurate lpi radar waveform recognition with cwd-tfa for deep convolutional network,” *IEEE Wireless Communications Letters*, vol. 10, pp. 1638–1642, 2021.

[15] Jie Yang, Yaoxiang Hui, and Junpeng Zhu, “Radar modulation recognition based on convolutional denoising autoencoder,” *Proceedings of the 2023 6th International Conference on Artificial Intelligence and Pattern Recognition*, 2023.

[16] Lai Shen, Daying Quan, Xiaofeng Wang, Xiaoping Jin, and Ning Jin, “Radar waveform recognition based on time-frequency images under deteriorating channel conditions,” *2022 IEEE 8th International Conference on Computer and Communications (ICCC)*, pp. 188–192, 2022.

[17] Yu Hong-hai, Yan Xiaopeng, Liu Shao-kun, Li Ping, and Hao Xinhong, “Radar emitter multi-label recognition based on residual network,” *Defence Technology*, 2021.

[18] Dongjin Li, Rui-juan Yang, Xiaobai Li, and Shengkun Zhu, “Radar signal modulation recognition based on deep joint learning,” *IEEE Access*, vol. 8, pp. 48515–48528, 2020.

[19] Zhiyu Qu, Lingjing Xu, and Qingbo Ji, “Unknown radar signal recognition method based on ser block and semi-hard triplet loss,” *2022 IEEE 5th International Conference on Electronic Information and Communication Technology (ICEICT)*, pp. 607–614, 2022.

[20] Sidra Ghayour Bhatti, Imtiaz Ahmad Taj, Mohsin Ullah, and Aamer Iqbal Bhatti, “Transformer-based models for intrapulse modulation recognition of radar waveforms,” *Eng. Appl. Artif. Intell.*, vol. 136, pp. 108989, 2024.

[21] Linh Manh Hoang, Minjun Kim, and Seung-Hyun Kong, “Automatic recognition of general lpi radar waveform using ssd and supplementary classifier,” *IEEE Transactions on Signal Processing*, vol. 67, pp. 3516–3530, 2019.

[22] Zhiyu Qu, Xiaojie Mao, and Zhian Deng, “Radar signal intra-pulse modulation recognition based on convolutional neural network,” *IEEE Access*, vol. 6, pp. 43874–43884, 2018.

[23] Chao Wang, Jian Wang, and Xudong Zhang, “Automatic radar waveform recognition based on time-frequency analysis and convolutional neural network,” *2017 IEEE International Conference on Acoustics, Speech and Signal Processing (ICASSP)*, pp. 2437–2441, 2017.

[24] Seung-Hyun Kong, Minjun Kim, Linh Manh Hoang, and Eunhui Kim, “Automatic lpi radar waveform recognition using cnn,” *IEEE Access*, vol. 6, pp. 4207–4219, 2018.

[25] Ming Zhang, Ming Diao, and Limin Guo, “Convolutional neural networks for automatic cognitive radio waveform recognition,” *IEEE Access*, vol. 5, pp. 11074–11082, 2017.

[26] Zeyu Tang, Hong Shen, and Chan Tong Lam, “Automatic recognition of dual-component radar signals based on deep learning,” *Sensors (Basel, Switzerland)*, vol. 25, 2025.

[27] Binbin Chen, Xudong Wang, Daiyin Zhu, He Yan, Guiguang Xu, and Ying Wen, “Lpi radar signals modulation recognition in complex multipath environment based on improved resnest,” *IEEE Transactions on Aerospace and Electronic Systems*, vol. 60, pp. 8887–8900, 2024.

[28] Liping Luo, Jie Huang, Yang Yang, and Dexiu Hu, “Radar waveform recognition with convnext and focal loss,” *IEEE Access*, vol. 12, pp. 171993–172003, 2024.

VII. COMPRESSED BENCHMARK ARCHITECTURES

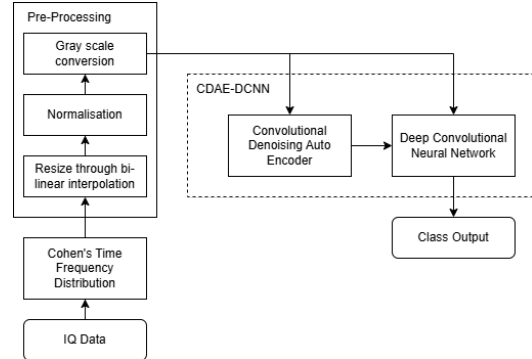


Fig. 7. Compressed architecture of CDAE-DCNN.

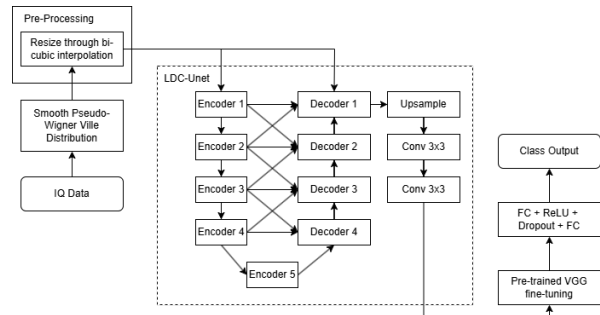


Fig. 8. Compressed architecture of LDC-Unet.

VIII. TABULAR FORMAT OF GRAPHS

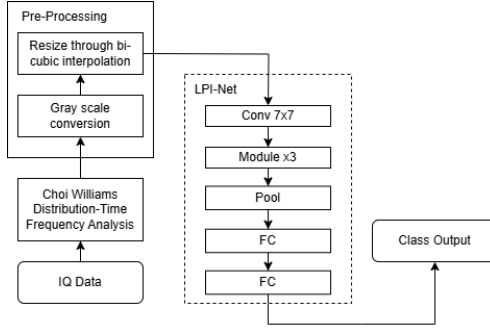


Fig. 9. Compressed architecture of LPI-Net.

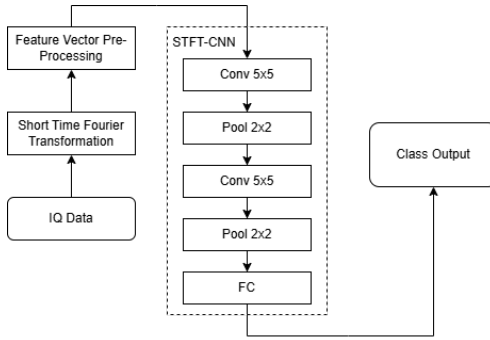


Fig. 10. Compressed architecture of STFT-CNN.

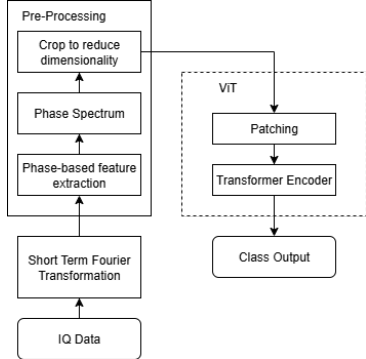


Fig. 11. Compressed architecture of ViT.

TABLE IV

ACCURACY (%) VS SNR (dB) FOR EXPERIMENT SNR(x):SNR(x),
USING ALL MODULATION TYPES. BEST VALUES PER ROW ARE IN BOLD.

SNR	STFT-CNN	LPI-Net	CDAE-DCNN	LDC-Unet	ViT
10	45.76	46.58	45.00	70.29	26.97
5	41.05	43.47	43.68	66.50	25.82
0	36.59	40.55	40.38	56.12	26.85
-2	38.27	39.97	40.14	50.95	29.20
-4	37.30	38.32	38.74	42.09	23.41
-6	35.80	37.82	38.39	42.15	25.08
-8	35.05	37.11	38.18	42.38	22.30
-10	33.33	34.80	37.89	42.33	3.03
-12	32.35	33.17	37.09	41.26	3.03
-14	31.92	29.67	35.92	41.76	3.03
-16	27.80	26.38	32.44	41.18	3.03
-18	26.20	18.26	29.73	41.21	2.95
-20	23.12	12.95	25.03	41.06	3.03

TABLE V

ACCURACY (%) VS SNR (dB) FOR EXPERIMENT SNR(ALL):SNR(x),
USING ALL MODULATION TYPES. BEST VALUES PER ROW ARE IN BOLD.

SNR	STFT-CNN	LPI-Net	CDAE-DCNN	LDC-Unet	ViT
10	44.94	45.18	44.74	71.59	44.21
5	44.94	45.48	44.39	68.42	43.76
0	42.76	43.42	42.50	62.70	43.18
-2	42.02	42.74	41.68	59.53	42.94
-4	41.80	41.92	40.94	55.17	42.86
-6	40.32	42.18	40.95	51.02	42.14
-8	38.64	41.08	40.26	48.35	42.26
-10	38.95	40.08	39.77	46.47	42.70
-12	37.67	38.18	40.00	44.59	41.59
-14	36.39	36.79	37.30	44.18	40.23
-16	33.65	33.98	36.12	43.59	38.91
-18	31.56	29.55	32.44	42.41	36.17
-20	25.48	19.61	25.03	41.85	29.48

TABLE VI

ACCURACY (%) VS SNR (dB) FOR EXPERIMENT SNR(x):SNR(x),
USING ONLY FREQUENCY MODULATION TYPES. BEST VALUES PER ROW
ARE IN BOLD.

SNR	STFT-CNN	LPI-Net	CDAE-DCNN	LDC-Unet	ViT
10	82.27	89.35	90.81	91.46	58.69
5	80.35	88.08	90.81	91.35	55.92
0	80.88	87.92	90.35	92.23	51.58
-2	76.58	87.65	90.04	91.96	46.96
-4	79.77	86.58	90.73	91.65	44.15
-6	77.12	85.62	90.15	91.92	48.04
-8	75.58	84.42	89.38	91.77	48.31
-10	74.46	80.96	88.08	91.23	40.38
-12	73.62	76.62	87.46	91.50	21.08
-14	67.81	69.65	85.50	91.42	15.96
-16	68.00	59.88	81.92	91.88	12.50
-18	59.92	40.00	75.46	90.85	9.31
-20	52.58	12.46	63.85	90.46	8.00

TABLE VII

ACCURACY (%) VS SNR (dB) FOR EXPERIMENT SNR(ALL):SNR(x),
USING ONLY FREQUENCY MODULATION TYPES. BEST VALUES PER ROW
ARE IN BOLD.

SNR	STFT-CNN	LPI-Net	CDAE-DCNN	LDC-Unet	ViT
10	88.81	91.31	91.12	92.50	91.96
5	89.19	91.00	91.65	91.92	91.31
0	85.92	91.54	91.88	91.85	91.46
-2	86.42	91.12	92.19	91.92	91.42
-4	85.88	90.73	92.31	92.50	92.00
-6	86.19	90.12	91.85	92.15	92.54
-8	84.42	90.12	91.27	92.35	91.46
-10	85.19	88.65	91.04	92.62	91.50
-12	83.46	86.23	90.31	92.08	89.35
-14	79.19	83.38	88.73	91.92	90.04
-16	78.23	75.88	86.04	91.77	88.38
-18	71.54	66.15	80.88	91.65	84.19
-20	60.15	47.19	67.08	90.81	75.04

IX. LIST OF ACRONYMS

TABLE VIII
INTRAPULSE MODULATION TYPES AND DESCRIPTIONS

Acronym	AIMC-Spec	Full Name	Description
UNMOD	✓	Unmodulated	Constant frequency, no modulation across the pulse duration.
LFM	✓	Linear Frequency Modulation	Frequency increases (LFM_up) or decreases (LFM_down) linearly across time (chirp).
NLFM	✓	Nonlinear Frequency Modulation	Frequency changes non-linearly to reduce sidelobes.
SFM	✓	Step Frequency Modulation	Discrete frequency steps within the pulse.
EQFM	✓	Equal-Width Frequency Modulation	Uniform sub-bands of frequency modulation.
DLFM	✓	Discrete Linear FM	Linear FM in discrete blocks, can be either up_down or down_up.
MLFM	✓	Modified Linear FM	Linear frequency modulation with nonlinear terms added to reduce sidelobes and enhance range resolution.
BFSK	✓	Binary Frequency Shift Keying	Equivalent to 2FSK; binary frequency hopping.
4FSK	✓	4-level Frequency Shift Keying	Switches between four frequencies.
FSK	✗	Frequency Shift Keying	General category of modulation using frequency switching.
SINFM	✗	Sinusoidal Frequency Modulation	Frequency follows a sinusoidal curve across time.
TRIFM	✗	Triangular Frequency Modulation	Symmetric linear up/down chirp within a pulse. AIMC-Spec considers DLFM_Up_Down as TriFM due to the single pulse classification task.
SCR	✗	Stepped Chirp	Sequence of chirps with stepped frequency offsets.
PCR3	✗	Piecewise Constant Ramp (3 segments)	Frequency ramps in fixed intervals across 3 segments.
QFSK	✗	Quadrature Frequency Shift Keying	Four FSK tones placed orthogonally.
BPSK	✓	Binary Phase Shift Keying	Phase alternates between two states (0, π).
QPSK	✓	Quadrature Phase Shift Keying	Phase modulated using four discrete values.
FRANK	✓	Frank Code	Polyphase code with linear phase progression.
BARKER	✓	Barker Code	Binary code with good autocorrelation properties. Consists of: 2_1, 2_2, 3, 4_1, 4_2, 5, 7, 11, 13
COSTAS	✓	Costas Code	Frequency-hopping sequence with good ambiguity properties.
P1-4	✓	P1-P4 Polyphase Codes	Four distinct polyphase modulation schemes designed for pulse compression, each offering specific autocorrelation properties and sidelobe control for improved range resolution.
EXP	✓	Exponential FM	Frequency varies exponentially over time.
T1-4	✗	T1-T4 Codes	Polyphase codes with tailored phase sequences for low sidelobes and Doppler tolerance, typically 16–100 chips long, similar to P1–P4 codes but optimized for Doppler performance.
LFM-BPSK	✓	LFM with BPSK	LFM chirp modulated with BPSK phase switching.
2FSK-BPSK	✓	2FSK with BPSK	2FSK combined with binary phase modulation.
LFM-SFM	✓	LFM with SFM	Hybrid of linear chirp and step frequency.
BPSK-LFM	✗	BPSK with LFM	BPSK applied over an LFM waveform.
EQFM-BPSK	✗	EQFM with BPSK	Phase modulated EQFM waveform.
EQFM-2FSK	✗	EQFM with 2FSK	Frequency hopping within EQFM envelope.
FRANK-EQFM	✗	Frank-coded EQFM	EQFM waveform modulated using Frank coding.
FRANK-4FSK	✗	Frank-coded 4FSK	4FSK with Frank phase coding.
LFM-4FSK	✗	LFM and 4FSK hybrid	Combines LFM's linear chirp with 4FSK's four discrete frequency steps to improve range resolution and interference rejection.
BPSK-FSK	✗	BPSK with FSK	Binary phase shift applied to FSK waveform.
FSK-LFM	✗	FSK with LFM	Frequency-hopping waveform with LFM characteristics.
FSK-BPSK	✗	FSK with BPSK	Frequency shift keyed waveform with binary phase.